AGU PUBLICATIONS

JGR

Journal of Geophysical Research: Biogeosciences

RESEARCH ARTICLE
10.1002/2016JG003441

**Key Points:**
- Rainfall seasonality across the Sahara desert is characterized on a yearly basis during 1998-2013
- Vegetation growing season can unfold during dry seasons after being initiated in rainy seasons
- The responses of land surface phenology to rainfall vary across different rainfall regimes

**Correspondence to:**
D. Yan,
dong.yan@sdstate.edu

**Citation:**
Yan, D., X. Zhang, Y. Yu, W. Guo, and N. P. Hanan (2016), Characterizing land surface phenology and responses to rainfall in the Sahara desert, *J. Geophys. Res. Biogeosci.*, *121*, 2243–2260, doi:10.1002/2016JG003441.

Received 5 APR 2016
Accepted 9 AUG 2016
Accepted article online 11 AUG 2016
Published online 29 AUG 2016



# Characterizing land surface phenology and responses to rainfall in the Sahara desert

**Dong Yan[1], Xiaoyang Zhang[1,2], Yunyue Yu[3], Wei Guo[4], and Niall P. Hanan[1]**

[1]Geospatial Sciences Center of Excellence, South Dakota State University, Brookings, South Dakota, USA, [2]Department of Geography, South Dakota State University, Brookings, South Dakota, USA, [3]NOAA/NESDIS/STAR, Camp Springs, Maryland, USA, [4]IMSG, NESDIS/STAR, College Park, Maryland, USA

**Abstract** Land surface phenology (LSP) in the Sahara desert is poorly understood due to the difficulty in detecting subtle variations in vegetation greenness. This study examined the spatial and temporal patterns of LSP and its responses to rainfall seasonality in the Sahara desert. We first generated daily two-band enhanced vegetation index (EVI2) from half-hourly observations acquired by the Spinning Enhanced Visible and Infrared Imager on board the Meteosat Second Generation series of geostationary satellites from 2006 to 2012. The EVI2 time series was used to retrieve LSP based on the Hybrid Piecewise Logistic Model. We further investigated the associations of spatial and temporal patterns in LSP with those in rainfall seasonality derived from the daily rainfall time series of the Tropical Rainfall Measurement Mission. Results show that the spatial shifts in the start of the vegetation growing season generally follow the rainy season onset that is controlled by the summer rainfall regime in the southern Sahara desert. In contrast, the end of the growing season significantly lags the end of the rainy season without any significant dependence. Vegetation growing season can unfold during the dry seasons after onset is triggered during rainy seasons. Vegetation growing season can be as long as 300 days or more in some areas and years. However, the EVI2 amplitude and accumulation across the Sahara region was very low indicating sparse vegetation as expected in desert regions. EVI2 amplitude and accumulated EVI2 strongly depended on rainfall received during the growing season and the preceding dormancy period.

## 1. Introduction

Deserts across the world have an area of approximately $52 \times 10^6$ km$^2$, which covers about 36% of the global land area [*Sagan et al*., 1979; *Shmida*, 1985]. The Sahara desert is the largest desert except those in the Polar Regions, which has profound impacts on both neighboring ecosystems and those far away from it. Specifically, dust emissions by the Sahara desert contribute to about 50–70% of the dust in the global atmosphere [*Safriel et al*., 2006], which dominates the supply of soil phosphorus for the Congo and Amazon Basins [*Okin et al*., 2004]. In addition, epidemic desert locust outbreaks in the Sahara desert can affect the Sahel, the Arabian Peninsula, and reach as far as India [*Safriel et al*., 2006]. Desert ecosystems are highly vulnerable to climate change since changes in temperature and rainfall may expose desert plant species to their physiological limits [*Tielbörger and Salguero-Gómez*, 2014]. The influences imposed by the Sahara desert on other ecosystems might be reinforced by the decreases in vegetation cover due to the projected increasing aridity in coming decades [*Safriel et al*., 2006].

Phenology of vegetation activity is one of the most effective indicators of vegetation responses to climate variability [*de Beurs and Henebry*, 2005; *Zhang et al*., 2007]. Land surface phenology (LSP) refers to the remotely sensed seasonal dynamics of vegetated land surfaces [*de Beurs and Henebry*, 2005]. LSP has been successfully retrieved and used to investigate the response of vegetation to climate variability in temperature-limited ecosystems in the Northern Hemisphere [*de Beurs and Henebry*, 2005; *Zhang et al*., 2007], the light-mediated Amazon rainforests [*Huete et al*., 2006; *Saleska et al*., 2007], and water-limited semiarid ecosystems across the globe [*Broich et al*., 2014; *de Beurs and Henebry*, 2008; *Heumann et al*., 2007; *Ma et al*., 2013; *Walker et al*., 2015; *Zhang et al*., 2005]. Previous studies on LSP changes in desert ecosystems have identified various anthropogenic and climatic drivers such as urbanization in southwestern U.S. [*Buyantuyev and Wu*, 2012], land management practices in Egypt [*Dall'Olmo and Karnieli*, 2002], and the changes in temperature and precipitation in central Asia [*Kariyeva and Van Leeuwen*, 2011]. Despite the profound impacts of the Sahara desert on other ecosystems, the knowledge of LSP across the Sahara desert is not available from the current regional and global scale LSP products [*Guan et al*., 2014a; *Vrieling et al*., 2013; *Zhang et al*., 2006], and there has been

no systematic analyses on the spatial and temporal patterns of LSP in the Sahara desert. This is due to the fact that the temporal variation of satellite-derived vegetation index is very subtle in desert regions, making LSP retrievals challenging [*Vrieling et al*., 2013; *Zhang et al*., 2005]. Previous remote sensing-based vegetation studies in the Sahara desert primarily focus on vegetation mapping to aid the control and forecast of desert locust outbreaks [*Pekel et al*., 2011; *Renier et al*., 2015]. The methods proposed by those studies provide information on the locations of green and dry vegetation at regular intervals, but other useful information such as the amplitude and duration of vegetation greenness is not available. Further, because of the highly variable rainfall, rainfall seasonality in the Sahara desert has not been well understood until recently when long-term satellite rainfall measurements become available [*Harada et al*., 2003; *Kelley*, 2014; *Liebmann et al*., 2012]. As a result, an understanding of LSP and its responses to rainfall seasonality across the Sahara desert is needed.

We retrieved LSP using the observations acquired by the Spinning Enhanced Visible and Infrared Imager (SEVIRI) on board the Meteosat Second Generation (MSG) series of geostationary satellites from 2006 to 2012 and analyzed rainfall seasonality measured by the Tropical Rainfall Measurement Mission (TRMM). We further examined the spatial and temporal patterns of LSP and rainfall. Finally, we investigated the responses of LSP to rainfall seasonality across different rainfall regimes.

## 2. Background

We focus on the region that lies between 15°N and 33°N in the Sahara desert of Africa (Figure 1), where maximum summer temperature can exceed 45°C [*Ali et al*., 2000] and annual rainfall increases from the eastern region to the northwestern and southern edges of the study area [*Liebmann et al*., 2012]. Dominant land cover in the study area includes sandy desert and dunes, stony deserts, and bare rocks [*Mayaux et al*., 2004] (Figure 1). Substantial vegetation can be found within irrigated agriculture sites (Figure 2a) and geomorphological features with relatively high soil moisture, such as dayas (Figure 2b), jebels (Figure 2c), chotts/sebkhas (Figure 2d), and wadis (Figure 2e). Dayas are shallow depressions which become temporary pools during the rainy seasons [*Mitchell and Willimott*, 1974]. Jebels (i.e., ranges of hills) primarily comprise inactive volcanoes and volcanic lava deposits, which have relatively moist environments due to the high elevations [*Burdette*, 2001]. Chotts and sebkhas together refer to saline wetlands that are flooded during rainy seasons [*Nedjimi*, 2012]. Sebkhas are the central saltwater zones, whereas chotts are succulent or halophytic plant dominated rings enclosing sebkhas [*Nedjimi et al*., 2012]. Wadis are wide riverbeds that are dry during most of the time but can be inundated after rain events [*Springuel et al*., 2006]. Jebels and wadis are widespread in the stony and rocky areas of the Sahara desert. In contrast, chotts/sebkhas and dayas primarily occur in northwestern Algeria and northern Libya, respectively. Irrigation agriculture can be found mainly in northern Algeria and Tunisia, central Libya, and northeastern Egypt.

To better articulate the relationship between LSP and rainfall seasonality, we divided the Sahara desert into three parts according to the dominant rainfall regime: the southern Sahara desert (SSD), northern Sahara desert (NSD), and central eastern Sahara desert (CESD) (Figure 1). Rainy season in SSD, NSD, and CESD is primarily controlled by the summer, winter, and spring rainfall regime, respectively [*Harada et al*., 2003; *Kelley*, 2014]. The method used to determine the dominant rainfall regime is presented in section 3.2. NSD generally occupies the region north of 26°N, whereas SSD is located across the southern edge of the study area. CESD is restricted to the region east of 10°E between 20°N and 26°N. Detailed descriptions of the rainfall regime in SSD, NSD, and CESD are presented in section 4.1.

## 3. Data and Methods

### 3.1. Rainfall Estimation From TRMM Product 3B42 and Bias Assessment

We used the daily rainfall time series acquired by the Tropical Rainfall Measurement Mission (TRMM) product 3B42 (post-real-time, Version 7) during 1998–2013 to investigate rainfall seasonality in the Sahara desert. The TRMM product 3B42 is available as 3-hourly rainfall rate (mm/h) with a spatial resolution of 0.25° covering the area between 50°N and 50°S. The Version 7 represents the most recent release of the TRMM 3B42 product generated based on the Multisatellite Precipitation Analysis (TMPA) algorithm [*Milewski et al*., 2015]. Daily rainfall was calculated as the sum of 3-hourly rainfall (mm) generated from the rainfall rate measurement. Previous evaluations indicate that the Version 7 TRMM product tends to overestimate rainfall in arid regions

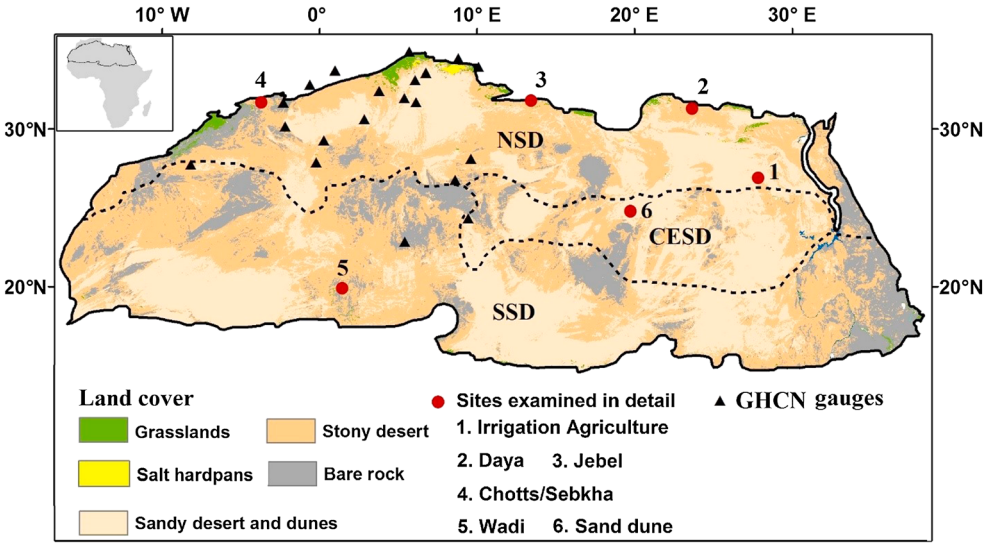


**Figure 1.** The dominant land cover in the Sahara desert. The red dots are the locations of selected sites for detailed examination of LSP and rainfall. The land cover information was retrieved from the Global Land Cover 2000 data set [*Mayaux et al.*, 2004]. Black triangles are the GHCN gauges that have relatively continuous daily rainfall records (annual missing data less than 5%) in at least 8 years during 1998–2013. Dashed black lines represent the approximate boundaries among the three dominant rainfall regimes.

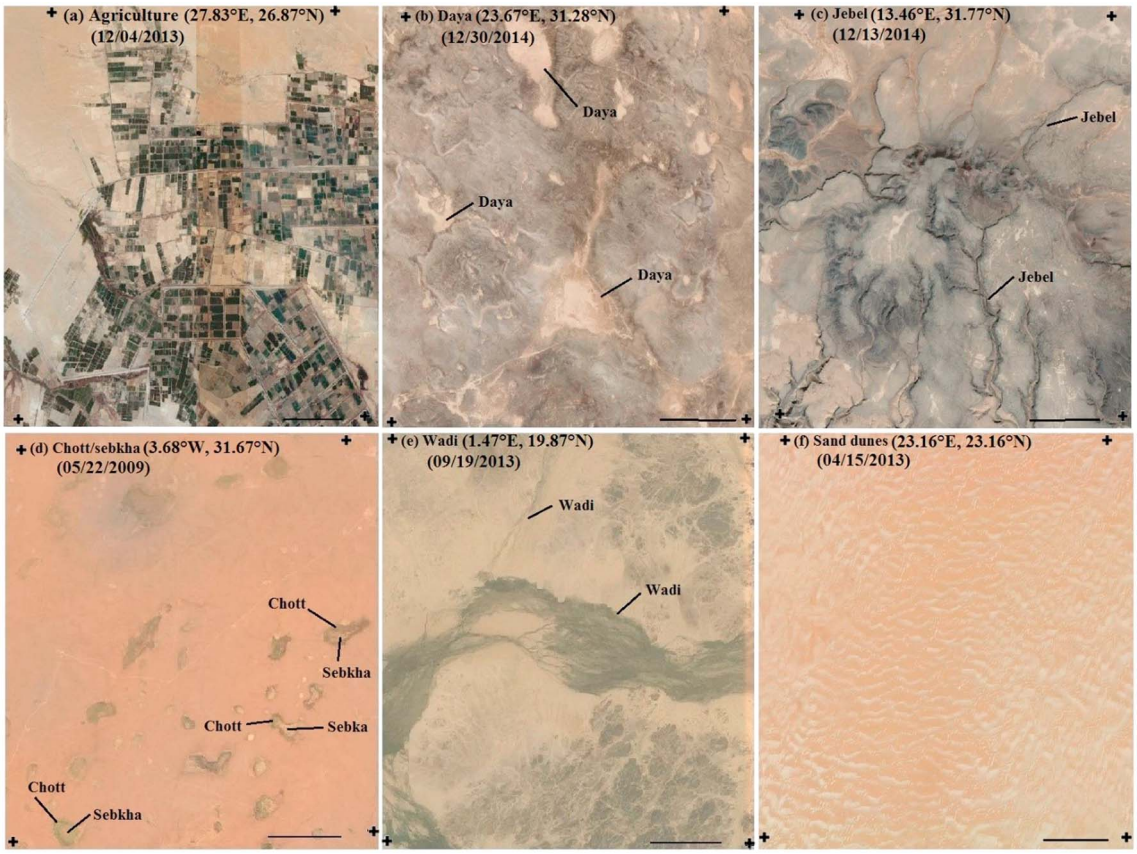


**Figure 2.** High-resolution satellite images obtained from Google Earth for (a) irrigation agriculture, (b) dayas, (c) jebels, (d) chotts/sebkhas, (e) wadis, and the (f) U.S. Geological Survey satellite calibration site. Black crosses represent the four corners of a 0.05° SEVIRI pixel. Location and acquisition date of each image are labeled at the upper left corner. Black bars in the lower right corners of images represent 1 km on the ground.

and the degree of overestimation decreases with the increases in the mean annual rainfall [*El Kenawy et al*., 2015; *Milewski et al*., 2015; *Peng et al*., 2014]. The overestimation is primarily attributed to the fact that the rainfall sensed by satellites tends to evaporate before reaching the ground surface [*Dinku et al*., 2010]. The bias reported for arid regions is 16% to 100% in northwestern China [*Peng et al*., 2014], between 25% and 50% in northeastern Spain [*El Kenawy et al*., 2015], and about 30% in northern Morocco [*Milewski et al*., 2015]. This high variation makes it difficult for us to directly adopt the reported bias in our study.

We investigated the bias of TRMM product 3B42 in the Sahara desert using daily rainfall measurements acquired by rain gauges during 1998–2013 from the National Oceanic and Atmospheric Administration's Global Historical Climatology Network (GHCN). We only used the daily rainfall data from 20 gauges that have at least 8 years' relatively complete records (i.e., the number of missing and bad quality daily rainfall records accounts for less than 5% in a specific year). Although these eligible gauges mainly fall in the northwestern Sahara desert (Figure 1), they provide a reasonable coverage of the mean annual rainfall gradient across the Sahara desert. For a given gauge, the relative bias in TRMM rainfall estimation was calculated using equation (1):

$$\text{Relative bias} = \frac{\sum_{i=1}^{N}(\text{TRMM}_i - \text{GHCN}_i)}{\sum_{i=1}^{N}\text{TRMM}_i} \times 100\% \quad (1)$$

where $\text{TRMM}_i$ and $\text{GHCN}_i$ represent the $i$th daily rainfall measurement by TRMM and a GHCN gauge, respectively. $N$ represents the total number of rainfall measurements during the years with relatively complete daily rainfall records.

We then used the relative bias to adjust the rainfall across the Sahara desert. Since the bias in TRMM rainfall measurements is a function of mean annual rainfall [*El Kenawy et al*., 2015; *Milewski et al*., 2015; *Peng et al*., 2014], we established an empirical model to link the relative bias to the TRMM mean annual rainfall according to the data from the 20 GHCN gauges. This model was applied to estimate the relative bias for each 0.25° grid cell based on the TRMM mean annual rainfall during 1998–2013. The daily TRMM rainfall time series during 1998–2013 in each 0.25° grid cell was then adjusted using the estimated relative bias based on equation (2):

$$A = O \times (1 - \text{Relative bias}) \quad (2)$$

where $O$ represented an original daily TRMM rainfall and $A$ is the adjusted daily rainfall.

### 3.2. Detection of Rainy Season From TRMM Product 3B42

Various rainy season retrieval methods have been proposed in the investigation of rainfall seasonality and its impacts on land surface phenology in Africa. For example, the rainy season start and end are determined when the accumulated rainfall exceeds a predefined percentage of the total rainfall in a climatological rainy season [*Guan et al*., 2014b; *Zhang et al*., 2005]. Alternatively, the rainy season is determined when a minimum amount of rainfall has been accumulated over a predefined duration of time [*Brown and de Beurs*, 2008]. In this study, we chose the Climatological Anomalous Accumulation (CAA) method [*Liebmann et al*., 2012] because it involves the fewest fixed thresholds. The minimum involvements of fixed thresholds can reduce the chances of obtaining false rainy season retrievals in the Sahara desert where the timing and amount of rainfall can vary greatly between locations and across years [*Kelley*, 2014].

We hereby briefly introduce the determination of the climatological and yearly onset (ORS) and end (ERS) of the rainy season by applying the CAA method to the bias-adjusted daily rainfall time series during 1998–2013. The climatological ORS and ERS at each 0.25° grid cell were determined in four steps. (1) A time series of daily average rainfall was generated by averaging rainfall obtained on the same day but from different years. (2) The daily mean rainfall was calculated as the mean value across the daily average rainfall time series. (3) An anomalous rainfall quantity was determined for each day of a year by subtracting the daily mean rainfall from the daily average rainfall. (4) A CAA time series was then generated by accumulating the anomalous rainfall quantity for each day starting from 1 January. The first day after the minimum and maximum CAA was determined as the climatological ORS and ERS, respectively. Note that the CAA calculation can begin at any day of a year and the alternation of the beginning date does not affect the determination of climatological ORS and ERS using the CAA method [*Liebmann et al*., 2012].

The yearly ORS and ERS in each 0.25° grid cell were retrieved based on the following procedures proposed by *Liebmann et al*. [2012]. (1) For each year, we determined a rainy season search interval, which begins at 50 days

ahead of the climatological ORS, and it continues to 50 days after the climatological ERS. This is to account for the variability in yearly ORS and ERS. (2) For each day within the search interval, we calculated an anomalous rainfall quantity by subtracting the climatological daily mean rainfall from the daily rainfall. (3) This anomalous rainfall quantity was accumulated throughout the search interval to generate the "anomalous accumulation" time series. (4) The first day after the minimum and maximum anomalous accumulation was determined as ORS and ERS, respectively. (5) The false ORS and ERS retrievals caused by short-lasted rain storms were removed using a recommended minimum rainy season duration of 5 days in arid areas [*Liebmann et al*., 2012]. We further calculated the mean values and standard deviations of ORS and ERS using the yearly ORS and ERS in the 0.25° grid cells where at least two yearly rainy seasons were detected between 2006 and 2012.

### 3.3. Generation of Time Series of Angularly Corrected Vegetation Index

The MSG series of geostationary satellites comprises four satellites (MSG-8, MSG-9 MSG-10, and MSG-11) located at a fixed position (0°N and 0°E). The SEVIRI on board MSG scans a full disk area every 15 min covering the entire Africa continent, most part of Europe, and eastern South America with a spatial resolution of approximately 3 km at nadir. In this study, we converted 30 min radiances from SEVIRI red and near-infrared channels acquired between 2005 and 2013 to top-of-atmosphere (TOA) reflectances using the methodology proposed by the *European Organisation for the Exploitation of Meteorological Satellites* [2012], and the cloud mask for each 30 min observation was determined using a Bayesian approach [*Merchant et al*., 2005].

To retrieve LSP over the study area, we generated angularly corrected two-band enhanced vegetation index (EVI2) every 30 min using the TOA reflectances of red and near-infrared channels [*Jiang et al*., 2008]. In order to eliminate the influences by the varying Sun-satellite geometry on EVI2, an empirical kernel-driven model [*Tian et al*., 2010] was applied to adjust each original 30 min EVI2 to a reference Sun-satellite geometry ($\theta_s = 45°$, $\theta_v = 45°$, $\phi = 90°$), in which $\theta_s$ is the solar zenith angle, $\theta_v$ is the satellite zenith angle, and $\phi$ is the Sun-satellite relative azimuth angle. The maximum value among the corrected 30 min EVI2 obtained within a day with solar zenith angle being less than 60° was used as the daily angularly corrected EVI2.

We further generated a 3 day composite EVI2 time series for each year between 2005 and 2013 to reduce the data volume and to retain the fine temporal resolution. For each 3 day period, the composited EVI2 was determined as the maximum EVI2 obtained after cloud-contaminated observations were excluded. Finally, we obtained 122 three-day EVI2 composites each year from 2005 to 2013. The quality of each 3 day SEVIRI EVI2 composite is described using a set of quality assurance (QA) flags, which are 0—clear, 1—cloudy, 2—bad input (i.e., solar zenith angle $>=60°$ or satellite zenith angle $>=60°$), and 3—water.

Across the Sahara desert, the pixel size of SEVIRI observation increases from the southwest (~4 × 4 km) to the northeast (~6 × 6 km) with the increases in the satellite zenith angle from approximately 30° at 18°W to about 50° at 30°E. We resampled the 3 day SEVIRI EVI2 composites to a fixed resolution of 0.05°. For each 0.05° grid cell, we first determined the majority QA category as the one with the highest number of pixels. We assigned the mean EVI2 of the majority QA category to a 0.05° grid, if the majority QA category was clear-sky condition. We followed the same procedure if the majority QA category was cloud contamination. We assigned a no-data value of −9999 to a 0.05° grid if the majority QA category was either bad input or water. The resampled EVI2 was also assigned QA flags of clear, cloudy, bad input, and water.

Since the temporal EVI2 variations are generally very subtle in the Sahara desert, it is very important to determine if such subtle variations are associated with the seasonal variation in solar zenith or azimuth angle. Our assumption is that if solar angle effects do exist, it would cause consistent seasonal variation in angularly corrected EVI2 even over nonvegetated surfaces. We correspondingly generated a 3 day time series of solar zenith angle and solar azimuth angle between 2006 and 2012 at a satellite calibration site (23.16°E, 23.16°N) used by the U.S. Geological Survey (Site 6 in Figure 1), which is covered by sand dunes in the southeastern Libyan desert (Figure 2f). More details of this calibration site are available at: http://calval.cr.usgs.gov/rst-resources/sites_catalog/radiometric-sites/libya-3/. The solar zenith angle and solar azimuth angle were calculated every 3 days at 12:00 P.M. UTC. For each year during 2006–2012, we examined the Pearson's correlation of good quality EVI2 (i.e., cloud-free EVI2) with solar zenith angle and solar azimuth angle, respectively. We further calculated the standard deviation of good quality EVI2 at this calibration site for each year during 2006–2012. We estimated the uncertainty in SEVIRI EVI2 to be 2 times as much as the maximum standard deviation in good quality EVI2 during 2006–2012 at this calibration site.

### 3.4. Detection of Land Surface Phenology

The onset and end of a growing season between 2006 and 2012 were detected from the 0.05° 3 day EVI2 time series using the Hybrid Piecewise Logistic Model (HPLM)-based LSP detection algorithm (HPLM-LSPD). The HPLM-LSPD was applied based on the following four steps [*Zhang*, 2015]: (1) For each year, we applied the HPLM-LSPD to a 3 day EVI2 time series with 244 composites acquired within a 2 year period: the preceding half year, the target year, and the succeeding half year; (2) we generated a smoothed 3 day EVI2 time series by eliminating gaps due to atmospheric contaminations and irregular values using the Savitzky–Golay filter and a local median filter; (3) a reconstructed EVI2 temporal trajectory was then obtained by fitting logistic curves to the smoothed EVI2 time series using HPLM; and (4) we determined the growing season onset and end between 2006 and 2012 based on the rate of change in the curvature of the reconstructed EVI2 temporal trajectory [*Zhang et al*., 2003]. We further calculated the EVI2 amplitude and the accumulated EVI2 during a growing season from the reconstructed EVI2 temporal trajectory. The EVI2 amplitude was calculated as the difference between the minimum and the maximum reconstructed EVI2 during a growing season. We adopted the EVI2 amplitude threshold method from a previous study [*Ma et al*., 2013] to determine if a detected growing season was potentially an artifact resulting from noises in SEVIRI data. Specifically, the retrieved LSP metrics were all ignored and excluded from further analyses if the SEVIRI EVI2 amplitude during a growing season was no higher than the uncertainty in EVI2. The accumulated EVI2 was calculated in two steps: (1) For a growing season, the difference between each reconstructed EVI2 and the minimum reconstructed EVI2 was calculated, and (2) the accumulated EVI2 was then calculated by accumulating the difference throughout the growing season. The accumulated EVI2 is a commonly adopted proxy for dryland vegetation productivity [*Broich et al*., 2014; *Zhang et al*., 2013]. Finally, we examined the duration, peak EVI2, EVI2 amplitude, and accumulated EVI2 during a growing season at sites 1–5 (Figures 1 and 2a–2e) to present the variation in LSP across the region in detail.

### 3.5. Investigation of LSP Responses to Rainfall

We investigated the responses of spatial shifts in LSP to those in rainfall using two groups of linear regression analyses. First, we investigated the associations of spatial patterns in EVI2 amplitude and accumulated EVI2 with those in the accumulated rainfall during a growing season (gRain) and the total rainfall received during a growing season and the preceding dormancy phase (tRain). The preceding dormancy phase refers to the period beginning at the end of the previous growing season until the onset of the current growing season. To achieve this, we resampled EVI2 amplitude and accumulated EVI2 to match rainfall data by assigning the mean value in EVI2 amplitude or accumulated EVI2 derived from the 25 0.05° grid cells to a 0.25° grid cell. We performed the linear regression analyses by using gRain or tRain as the predictor variable and EVI2 amplitude or accumulated EVI2 as the response variable in each year during 2006–2012. The regression analyses were also repeated using the mean values of gRain, tRain, EVI2 amplitude, and accumulated EVI2 during 2006–2012.

The second group of regression analyses was to determine the associations of spatial shifts in the onset and end timings of growing season with the timings of ORS and ERS, respectively. The onset and end of a growing season were spatially aggregated using a majority sampling method, which assigns the dates of onset or end with the most frequent occurrences among the 25 0.05° grid cells to the enclosing 0.25° grid cell. We used the majority sampling method instead of simply using the mean value of the 25 0.05°grid cells because there can be abrupt changes in the onset and end timings of growing season among neighboring 0.05° grid cells, which can result in seriously skewed mean values due to the presence of a few irregular values. For each year during 2006–2012, the yearly ORS was used as the predictor variable, whereas the yearly growing season onset was used as the response variable. We also examined the regression between the mean value of ORS during 2006–2012 and that of growing season onset. The regression analyses were performed with the Sahara desert as a whole and separately for NSD, SSD, and CESD. Those regression analyses were repeated with the yearly or mean ERS as the predictor variable and the yearly or mean growing season end as the response variable.

Note that all the regression analyses were conducted in the nonagriculture regions of the Sahara desert. We excluded the 0.25° grid cells in which agriculture was present by an exhaustive search on high-resolution Google Earth images. A total of 208 0.25° grid cells were identified and subsequently excluded from the regression analyses.

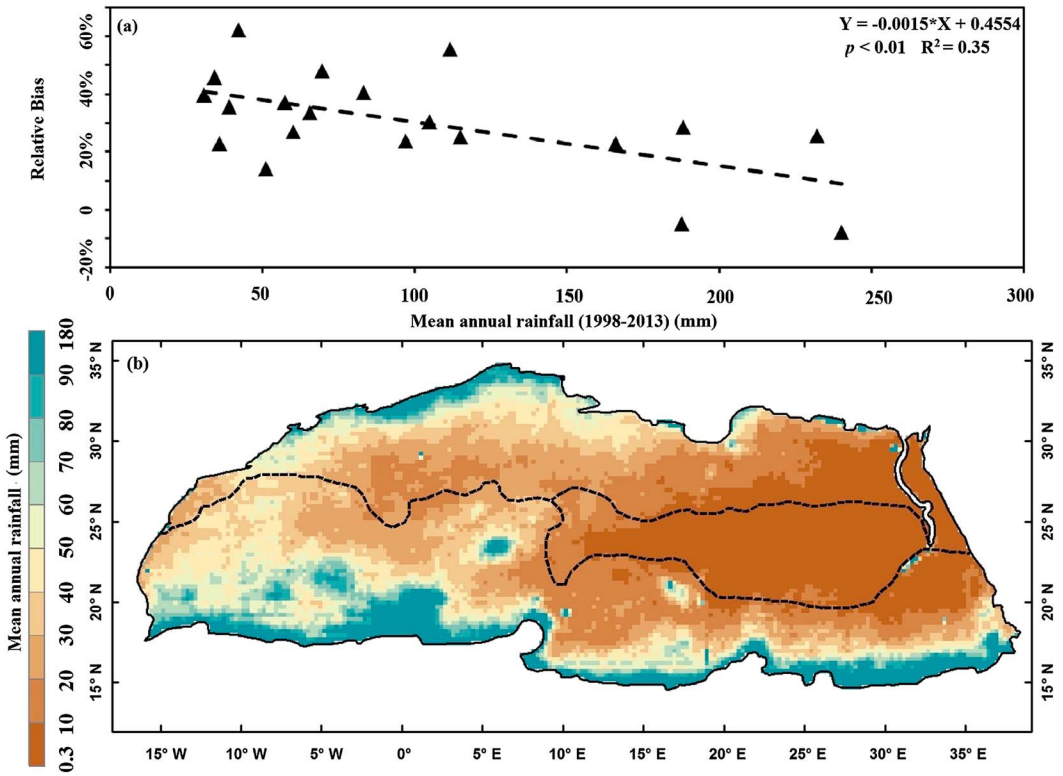


**Figure 3.** The bias assessment of TRMM rainfall. (a) The variation in relative bias as a function of the original TRMM mean annual rainfall and (b) the adjusted TRMM mean annual rainfall during 1998–2013.

## 4. Results

### 4.1. The Bias Assessment of TRMM Rainfall Data and the Spatial Variations in Rainfall Seasonality

Figure 3 shows the variations in the relative bias with the original TRMM mean annual rainfall and the spatial pattern of the adjusted mean annual rainfall during 1998–2013. With the variation in the original TRMM mean annual rainfall increasing from 30.8 mm to 240.2 mm, the relative bias decreased from 62.30% to −7.78% among the 20 GHCN gauges. The regression was significant at $p < 0.01$ with a $R^2$ of 0.35. The spatial distribution of mean annual rainfall shows that the rainfall was below 60 mm in about 82% the region. The mean annual rainfall was very low (i.e., less than 10 mm) across much of CESD and the surrounding areas. It was relatively high along the northwestern and southern edges of the Sahara desert, which could vary between 90 mm and 180 mm.

Figure 4 illustrates the climatological ORS and ERS and the corresponding CAA values during 1998–2013 in the four typical cases. Specifically, the climatological ORS and ERS occurred in June and late September (summer rainy season), respectively, with a rainy season duration of 115 days and a daily mean rainfall of 0.41 mm in the wadi grid cell. The corresponding minimum and maximum CAA was −56.62 mm and 33.13 mm, respectively. In contrast, ORS varied from September to December, and ERS shifted from late November to the following May (winter rainy season) with a rainy season duration between 87 and 202 days at the other three sites. The related minimum CAA, maximum CAA, and daily mean rainfall ranged from −14.78 mm to −3.42 mm, from 4.37 mm to 6.28 mm, and from 0.06 mm to 0.21 mm, respectively.

Figure 5 demonstrates the yearly ORS and ERS during 2006–2012 in the four typical cases. Except the daya grid cell where rainfall occurred as isolated rain storms that spread widely apart, rainfall in the other three grid cells revealed a relatively distinct seasonality. The average rainy season duration increased from 54 days in the daya grid cell to 90 days in the wadi grid cell. However, the rainy season duration varied greatly in the daya grid cell from less than 20 days during 2008–2010 to more than 100 days in 2007 and 2011. The interannual variation was much lower in the other three grid cells with a maximum standard deviation of 27 days

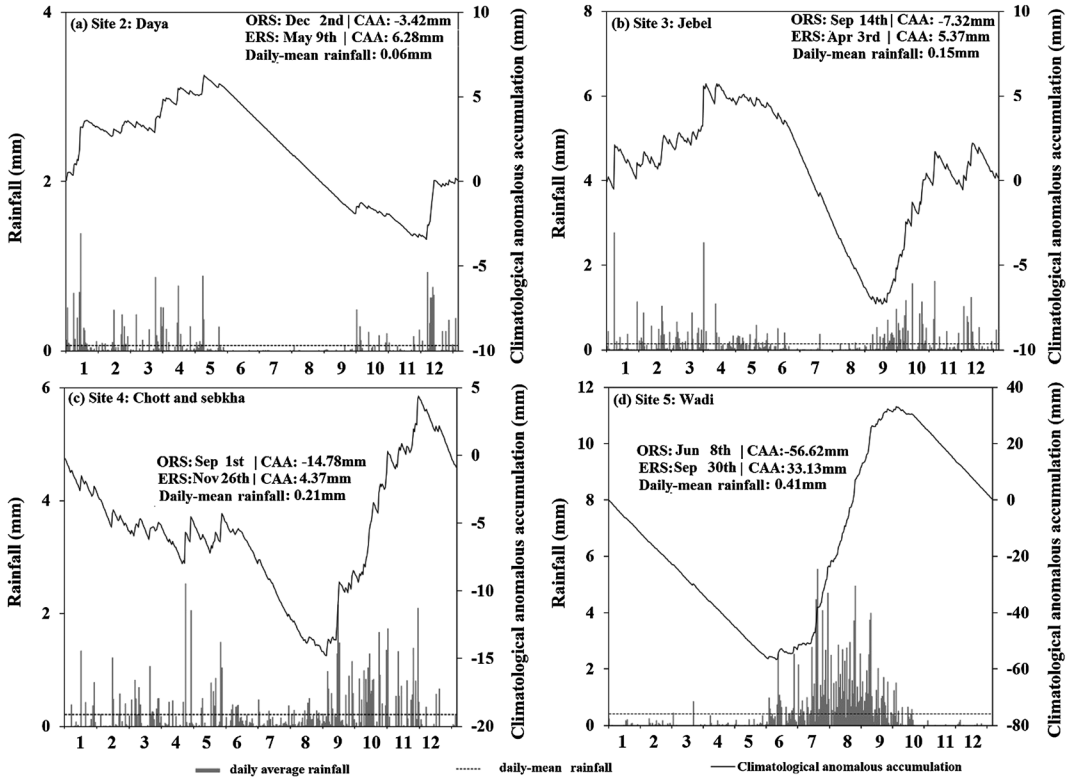


**Figure 4.** The climatological daily average rainfall, daily mean rainfall, and rainy season (ORS and ERS) during 1998–2013 in the four typical cases.

during 2006–2012. Yearly rainy season was not detectable in 2007 in the chott/sebkha grid cell and between 2011 and 2012 in both the daya and jebel grid cells.

Figure 6 shows the spatial variations in the mean and standard deviations of ORS and ERS during 2006–2012. Rainy seasons were consistently detected in western CESD and across much of NSD and SSD (i.e., at least two yearly rainy seasons were detected during 2006–2012). In NSD, the mean ORS generally shifted from around mid-August in the west to the following mid-February in the east, and it occurred as late as mid-March between 0° and 10°E in the southern NSD. The mean ERS varied accordingly from early November to mid-May. Despite the significant changes in the mean ORS and ERS across NSD, we characterized NSD as a single region because the changes in ORS and ERS across NSD were generally consistent with each other, which are believed to be caused by a single atmospheric system traveling along the west-east direction (details are provided in section 5.1) [*Harada et al*., 2003]. In SSD, the mean ORS was earlier in the south relative to the north of the region. Specifically, ORS occurred between late June and mid-September. The spatial changes in mean ERS differed between the western and eastern SSD. In eastern SSD (east of 10°E), ERS varied between mid-August and mid-September from north to south, whereas ERS occurred during mid-October over much of the western SSD. In CESD, the mean ORS occurred around late April followed by ERS around mid-June. The length of rainy season was about 1 to 3 months in NSD and SSD and about 1.5 month in CESD. The standard deviation in ORS and ERS was higher in NSD than that in SSD and CESD. For ORS, the standard deviation was predominantly less than 45 days in SSD and CESD, whereas it varied from 30 to 60 days across much of NSD and over 60 days in northwestern NSD. The spatial pattern was similar for the standard deviation in ERS.

### 4.2. Assessments of Solar Angle Effects on EVI2 Temporal Variations

Figure 7 shows the temporal variations in solar zenith angle, solar azimuth angle, and EVI2 between 2006 and 2012 at the satellite calibration site. The variations in solar angles showed strong seasonal patterns. The solar zenith angle reached the minimum of just over 20° around mid-July and the maximum of about 52° during

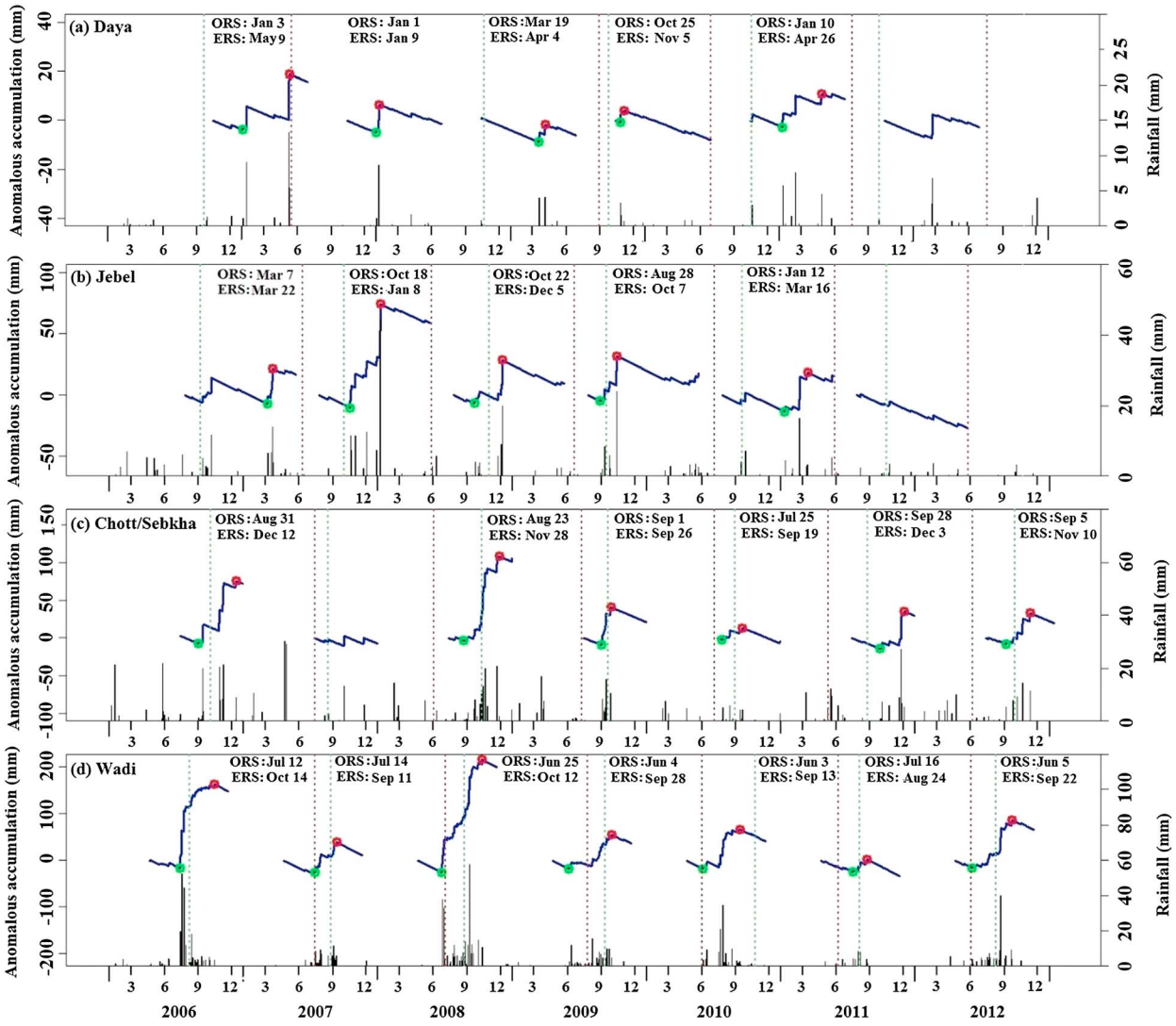


**Figure 5.** The daily rainfall and yearly ORS and ERS from 2006 to 2012 in the four typical cases. Green circle: ORS, red circle: ERS, solid blue line: the anomalous accumulation time series (left *Y* axis), black bar: daily rainfall (right *Y* axis), green dashed line: aggregated growing season onset, and red dashed line: aggregated growing season end.

mid-December, whereas the solar azimuth angle decreased from the maximum of about 275° in late June to the minimum of about 206° around mid-January in the next year. In contrast, the original angularly corrected EVI2 varied within the range between 0.04 and 0.12 without distinct seasonal patterns. The results of the correlation analyses indicated that EVI2 was not significantly correlated with either solar zenith angle or solar azimuth angle ($p > 0.1$) in 2006, 2008, and 2009, although the correlation was significant ($p < 0.1$) in the other 4 years. This indicates that changes in EVI2 were limitedly affected by the residual effects of solar angle changes that were not completely eliminated using the angular correction model. During 2006–2012, the maximum standard deviation of good quality EVI2 at the calibration site occurred in 2006 with a value of 0.01 EVI2 units; we thus estimated the uncertainty in SEVIRI EVI2 to be 0.02 EVI2 units. If the amplitude of a retrieved growing season was higher than 0.02, the growing season is unlikely an artifact resulting from changes in solar angles.

### 4.3. Spatial Patterns in LSP

Figure 8 shows the temporal trajectories of the original and the reconstructed phenological time series at an irrigation agriculture site and four typical geomorphological feature sites. Compared with the four

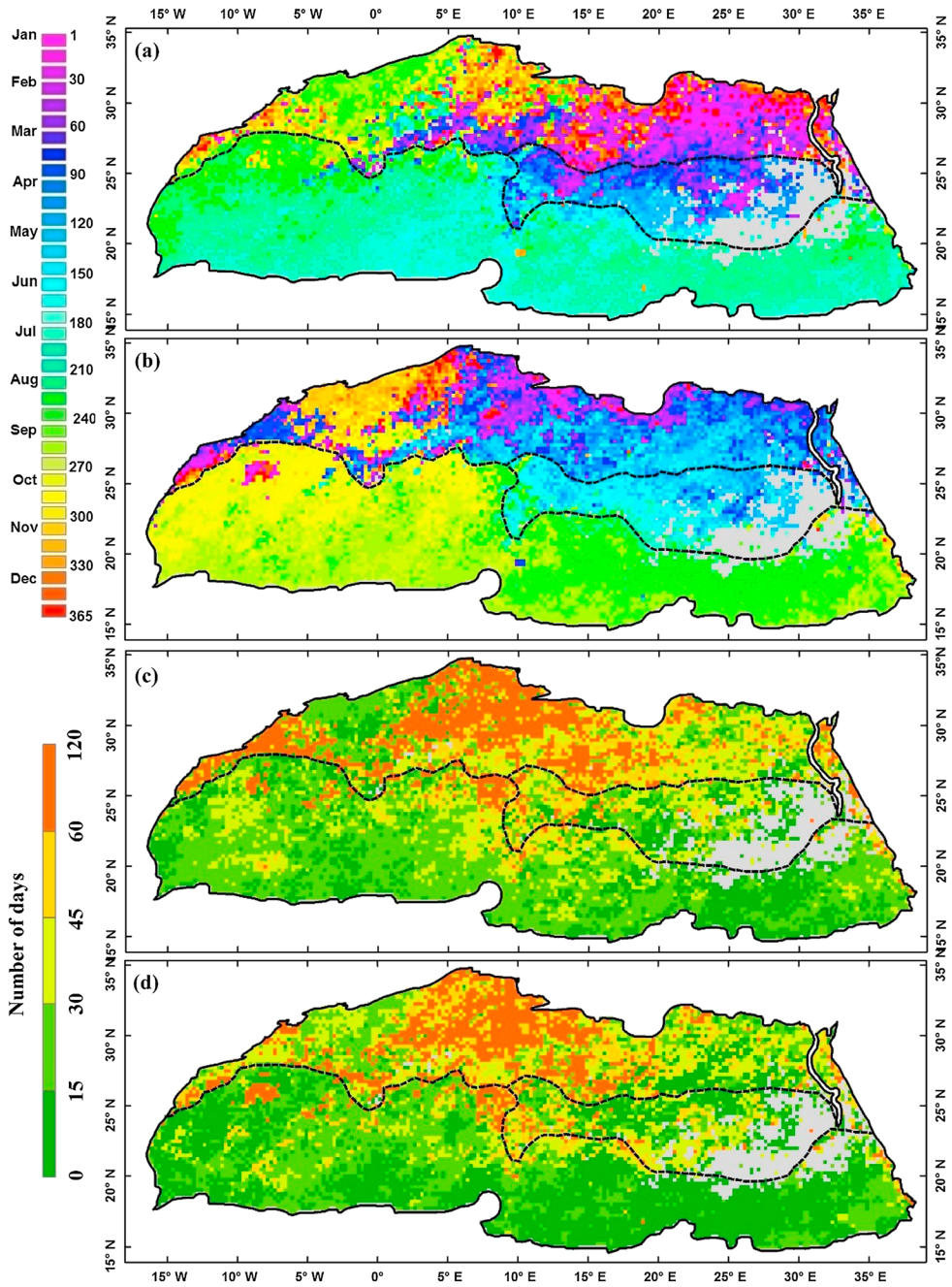


**Figure 6.** Variation in rainy season timings during 2002–2006. Grey color represents the area where less than two rainy seasons were retrieved during 2006–2012. Dashed black lines represent the approximate boundaries among the three dominant rainfall regimes. (a) Mean ORS, (b) mean ERS, (c) standard deviation in ORS, and (d) standard deviation in ERS.

geomorphological feature sites, the irrigation agriculture site revealed the shortest duration of growing season but the highest EVI2 values (i.e., peak EVI2, EVI2 amplitude, and accumulated EVI2) in all the 7 years (except EVI2 amplitude during 2008–2009 and accumulated EVI2 during 2006–2007 and 2008–2009). Consistent differences in peak EVI2 and EVI2 amplitude were found between some geomorphological feature sites during certain years. Specifically, peak EVI2 was higher in the chott/sebkha and jebel sites than that in the wadi and daya sites in all the 7 years, and the average peak EVI2 varied from 0.11 in the wadi site to 0.16 in the chott/sebkha site. Similarly, the EVI2 amplitude in the chott/sebkha and jebel sites was almost always higher than that in the wadi and daya sites (only except in 2006–2007).

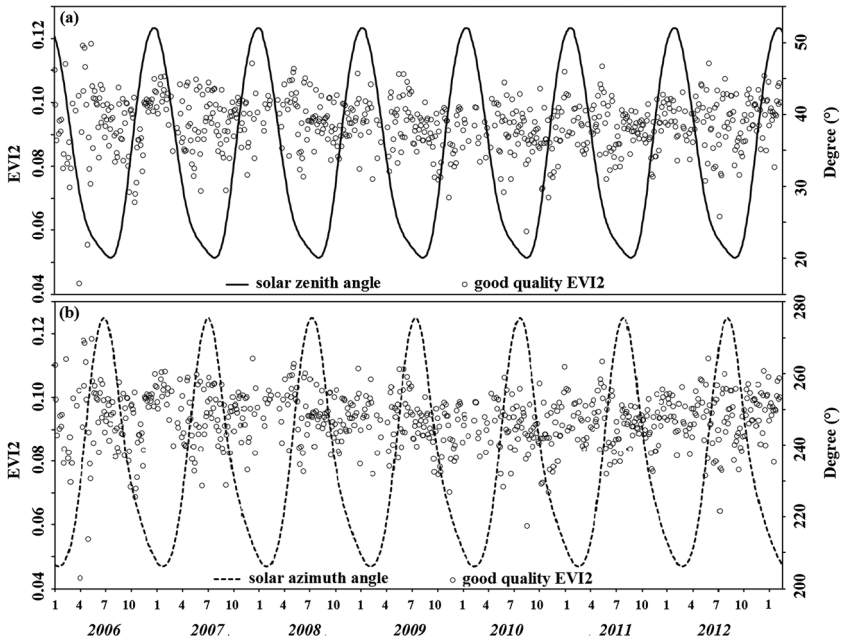


**Figure 7.** Temporal variation in solar zenith angle, solar azimuth, and original angularly corrected EVI2 at the satellite calibration site between 2006 and 2012. The solid line in Figure 7a represents solar zenith angle, and the dashed line in Figure 7b is solar azimuth angle. Black circles represent the original angularly corrected EVI2 obtained under cloud-free conditions.

The average EVI2 amplitude ranged from 0.03 in the daya site to 0.06 in the chott/sebkha site. The duration of growing season was the longest in the wadi site except during 2007–2008 and 2009–2010. The average duration varied from 250 days in the jebel site to 304 days in the wadi site. The accumulated EVI2 varied greatly between sites and across years. The maximum value of accumulated EVI2 was 4.30 in the chott/sebkha site during 2008–2009, whereas the minimum value was 1.06 in the daya site during 2007–2008.

Figure 9 displays the spatial variations in the mean timings of growing season onset and end and their standard deviations. In SSD, the mean timing of growing season onset spatially shifted from early August around 16°N to between mid-September and early October around 26°N, while the mean timing of growing season end was generally between June and early September in the next year except at some isolated areas where growing season end was as early as mid-May. In NSD, the mean timing of growing season onset varied from as early as mid-August at 10°W to late November between 25°E and 30°E, and the mean timing of growing season end was around late June in the northwestern and central regions, but it could be as late as in August in the southwestern and northeastern regions. Consistent vegetation growing seasons (i.e., at least four growing seasons were detected) were only detected at a few isolated pixel locations across CESD during 2006–2012. The standard deviations in both growing season onset and end were less than 30 days over much of NSD and SSD. The high variation in growing season timings was only found in a narrow stripe within southern SSD between 10°E and 20°E, where the standard deviation varied between 30 and 60 days in ORS, whereas it was predominantly over 60 days in ERS.

### 4.4. Responses of LSP to Rainfall Seasonality

The relationships between timings of LSP and rainy seasons in the four geomorphological feature sites were examined by comparing the timings of yearly growing season and that of yearly rainy season shown in Figure 5. Overall, the rainy seasons were much shorter than growing seasons. However, while ERS generally preceded the growing season ends, the relationship between ORS and growing season onset varied between sites and across years. Specifically, ORS occurred after growing season onsets in the daya site, whereas ORS preceded growing season onsets in the chott/sebkha and wadi sites (except during 2011 in the chott/sebkha

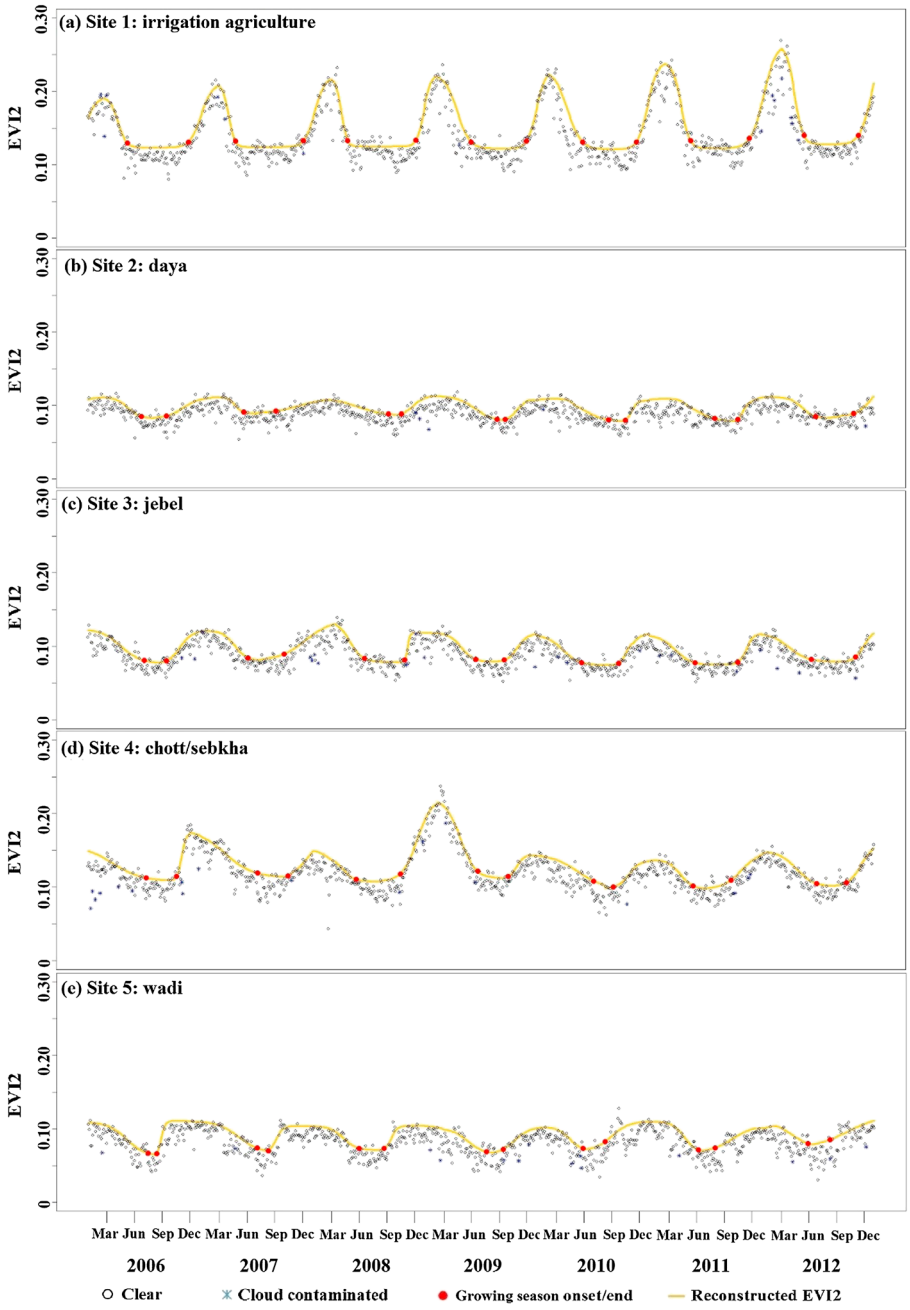


**Figure 8.** The temporal trajectories of original and reconstructed EVI2 time series. Red dots on the ascending and descending phase of an EVI2 trajectory represent the onset and end of a growing season, respectively.

site). In the jebel site, the ORS lagged the growing season onsets for more than 5 months in 2007 and 2011, whereas it occurred shortly before the growing season onsets during 2008–2009.

The regression analyses indicated that the timing of LSP was complexly associated with that of the rainy seasons across the Sahara desert. Overall, the response of growing season onset to ORS was stronger than that of growing season end to ERS and the response of growing season onset to ORS was stronger in SSD than that in NSD. Specifically, no significant relationship between the timings of LSP and rainy seasons was identified during 2006–2012 in NSD. In SSD, mean growing season onset was significantly associated with mean ORS ($p < 0.001$, $R^2 = 0.10$) with a residual standard error (RSE) of about 15 days.

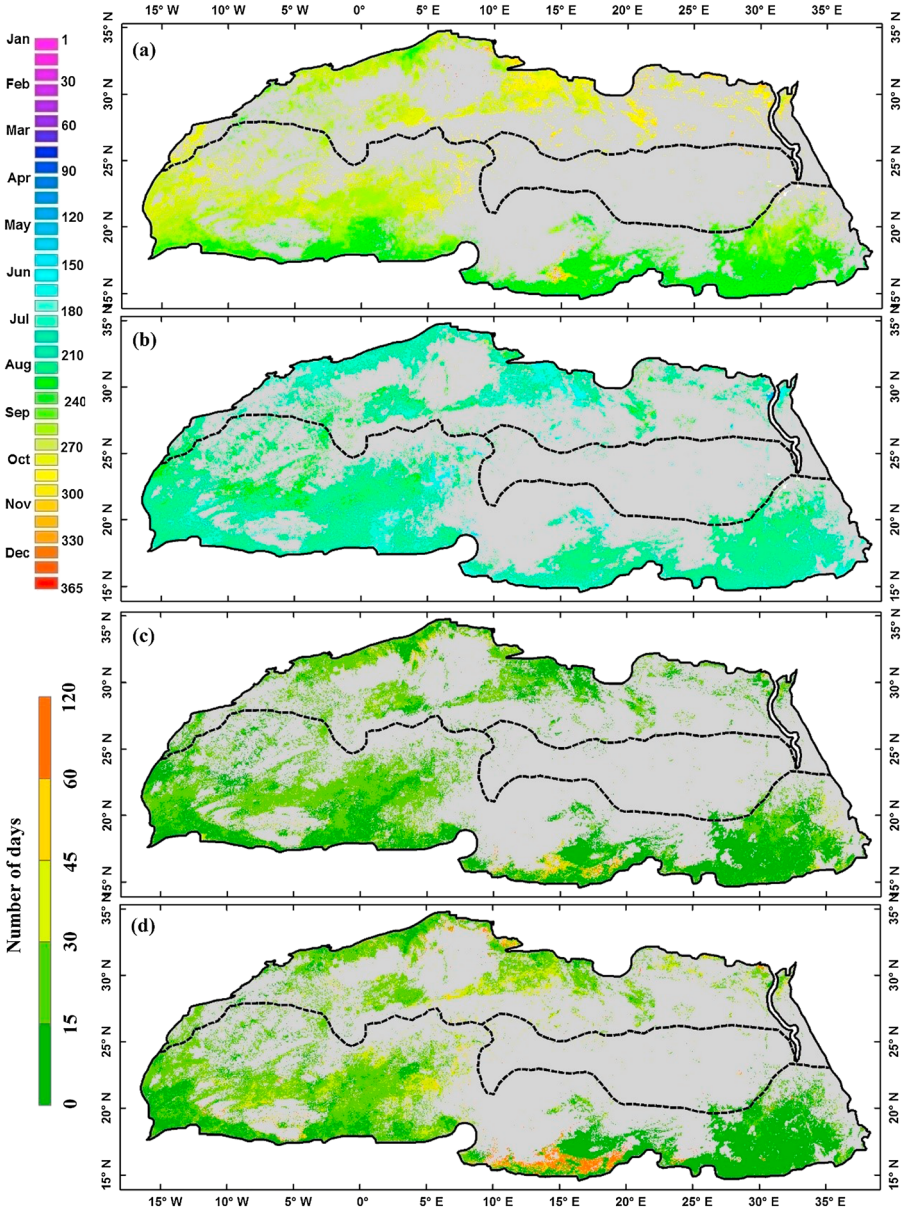


**Figure 9.** Spatial variation in mean values between 2006 and 2012 for growing season (a) onset timing and (b) end timing and the standard deviations in (c) growing season onset and the (d) growing season end. The grey color represents the areas where the number of detectable growing seasons (i.e., EVI2 amplitude > 0.02 EVI2 units) between 2006 and 2012 was less than 4.

However, the significant relationship between growing season onset and ORS during individual years was only found in 2007 ($p < 0.001$, $R^2 = 0.14$, and RSE = 12 days) and 2012 ($p < 0.001$, $R^2 = 0.12$, and RSE = 27 days). Note that since consistent growing seasons were only detected at a few pixels across CESD (Figure 9), the examination of the relationship between timings of LSP and rainy seasons across CESD was omitted.

Figure 10 presents the regressions between LSP magnitudes (i.e., accumulated EVI2 and EVI2 amplitude) and rainfall accumulations (i.e., gRain and tRain) during 2006–2012. Overall, LSP magnitudes significantly increased with rainfall accumulation ($p < 0.001$) in individual years. However, both accumulated EVI2 and EVI2 amplitude were more strongly associated with tRain with higher $R^2$ and smaller RSE than with gRain.

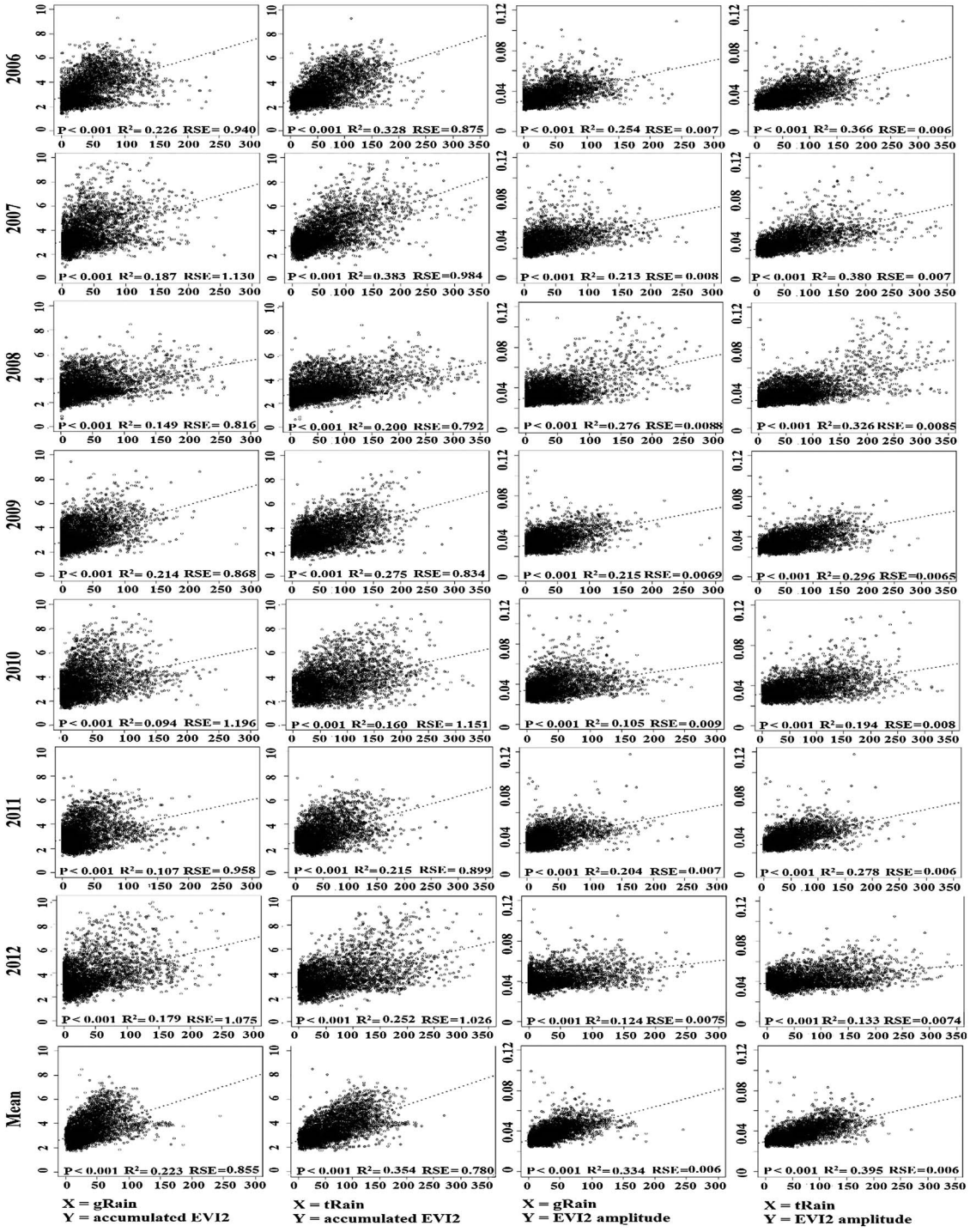


**Figure 10.** Variations in LSP magnitudes (accumulated EVI2 and EVI2 amplitude) with rainfall accumulation (gRain and tRain) during 2006–2012.

On the other hand, EVI2 amplitude was more sensitive to either gRain or tRain with higher $R^2$ and smaller RSE than accumulated EVI2 was, except during 2012. Similarly, the mean LSP magnitudes also significantly increased with the mean rainfall accumulations during 2006–2012, but the relationships were much stronger than those from individual years except between accumulated EVI2 and gRain in 2006 and between accumulated EVI2 and tRain in 2008.

## 5. Discussions

### 5.1. The Atmospheric Influences on Rainy Seasons and the Determination of Rainy Season

Rainy seasons in NSD, SSD, and CESD are under the influences of different atmospheric systems. In NSD, the extratropical rainfall resulting from a midlatitude westerly triggers ORS [*Harada et al*., 2003; *Nicholson*, 2000]. Following the movement of the westerly, the mean ORS reveals an eastward shift from mid-August to the following mid-February. The winter rainy season in NSD lasts about 1 to 3 months before ERS begins to unfold between early November and the following mid-May. In SSD, the timing of ORS and ERS is associated with northward and southward movements of the Intertropical Convergence Zone (ITCZ), respectively. The ITCZ arrives at the southern region of SSD around late June and continues to move northward until it reaches its northern limits in mid-September [*Harada et al*., 2003; *Nicholson*, 2000]. ITCZ then starts to retreat southward and eventually moves to the south of the SSD by mid-October. The distinct summer rainy season in SSD is short, the length of which generally varies from 1 month in the northwestern region to about 3 months in the southeastern region. In CESD, the spring rainy season unfolds between late April and mid-June, which is believed to be controlled by a midlatitude trough together with tropical disturbances [*Kelley*, 2014; *Nicholson*, 1981, 2000].

The determination of yearly rainy season is very challenging in the Sahara desert because the timing and amount of rainfall are very irregular. The CAA method is capable of capturing the major component of the yearly rainy season. In SSD, since rainfall events had relatively distinct seasonality and were not separated by prolonged dry periods, the yearly rainy seasons were reasonably detected using the CAA method. For example, the yearly rainy seasons in the wadi grid cell were accurately characterized despite the high interannual variations in total rainfall. In contrast, due to the high variability in rainfall timing within NSD, the rainfall time series could either have a unimodal or a bimodal distribution in individual years. The CAA method either only captured the major rainy season (e.g., Figure 5b in 2006 and 2011) or it captured both but including a relatively long dry spell (e.g., Figure 5a in 2007), because the CAA method is proposed to deal with the unimodal distribution [*Liebmann et al*., 2012]. Since rainfall was extremely scarce in the eastern portion of CESD, which is the driest part of the Sahara desert [*Kelley*, 2014], no consistent rainy seasons were detectable in this region. Clearly, further research is needed to effectively characterize the yearly rainy season in NSD where the timing of daily rainfall is highly variable, but the development of such a method is beyond the scope of this research. Alternatively, it might be more practical to characterize yearly rainy seasons in NSD and CESD with the time scale of a month or a longer period of time [*Kelley*, 2014] rather than determining the onset or end of a rainy season as a specific day of year. In spite of the challenges, the spatial pattern in both the retrieved mean timing and length of rainy season generally agree with those identified in previous studies [*Harada et al*., 2003; *Kelley*, 2014; *Liebmann et al*., 2012; *Nicholson*, 2000].

### 5.2. The Influences of Geomorphological Feature on Land Surface Phenology

In the Sahara desert, vegetation growing season can be as long as 300 days or more in some areas and years, although the EVI2 amplitude and accumulated EVI2 tend to be very low indicating sparse vegetation as expected in desert regions. Long growing seasons ( i.e., over 300 days) have also been reported by a previous study on the dry savannas dominated by Acacia woodlands/shrublands in northern Australia with mean annual rainfall between 300 mm and 400 mm [*Ma et al*., 2013]. In contrast, the temporal overlap between vegetation growing season and rainy season is relatively short and varies across rainfall regimes. In NSD, vegetation growing season overlapped rainy season during September–November and December–May in the western and eastern regions, respectively. In SSD, the overlap was generally no more than 2 months between July and October. The short overlap indicates that vegetation growing season predominately unfolded during the dry season. According to the characteristics of LSP and rainy season presented for the four geomorphological feature sites, it is suggested that vegetation growth was likely influenced by geomorphological features which controlled soil moisture accumulations. This influence has been reported by previous studies. Specifically, relatively high vegetation greenness was found in wadis, dayas, chotts/sebkhas, and jebels within the stony and rocky regions where runoff could concentrate rainfall and thus maintain soil moisture for a longer period of time than in the surrounding areas [*Springuel et al*., 2006], supporting deep-rooted woody species [*Ali et al*., 2000]. Previous studies show that soil moisture as low as 4% could be maintained at the depth of 40–50 cm for more than half a year in the low land area of wadi channels [*Springuel et al*., 2006], and some perennial plants were able to sustain growth with the stored

moisture for more than a year [*Ali et al*., 2000]. Dayas receive rainfall runoff from large drainage basins through wadi channels [*Benhouhou et al*., 2003]. The surface deposits in dayas could form dry layers that can significantly reduce the loss of moisture kept in deeper soil profiles [*Benhouhou et al*., 2003]. Water depths in chotts/sebkhas are generally lower than those in dayas and chotts/sebkhas mainly benefit from their endorheic nature to accumulate rainfall water [*Nedjimi et al*., 2012]. With shallow soils, mountainous areas of the Sahara desert could support large shrubs with moisture trapped in rock cracks [*Benhouhou et al*., 2003]. Perennial plants living in rocky areas have been found to develop flexible exploring roots enabling them to utilize soil moisture trapped in soil and rock cracks by penetrating cracks or going through extremely complex paths [*Noy-Meir*, 1973]. These mechanisms of moisture accumulation might have impacts on the LSP characteristics. For example, the peak EVI2 and EVI2 amplitude were consistently lower in the daya and wadi sites than in the chott/sebkha and jebel sites during 2006–2012.

### 5.3. The Responses of Land Surface Phenology to the Rainy Seasons

Vegetation growth is primarily constrained by the availability of water in dryland ecosystems, but the responses of LSP timing and magnitude to the rainy seasons are complex and vary across rainfall regimes. Our results revealed a stronger response of growing season onset to ORS than that of growing season end to ERS. Growing season onset occurred after ORS across much of SSD. This is consistent with the results from a previous field-based study on desert plant phenology, in which a strong dependence in growing season onset timing for both annual and perennial desert plants on the timing of rainfall is identified [*Sakkir et al*., 2015]. However, the significant relationship between growing season onset and ORS was inconsistent according to yearly data. This is likely caused by the high variability in the initial rainfall accumulation around ORS in individual years. For example, the rainfall accumulation around ORS could be very low in some years so that it would need a longer time or even fail to trigger the growing season onset. In NSD, rainfall events frequently occurred in an isolated manner without distinct seasonality, so that it is difficult to accurately characterize the yearly rainy season. As a result, no significant relationship was identified between growing season onset and ORS. However, rainfall seemed to occur predominately during growing seasons. For example, the majority of the isolated rain storms coincided with growing seasons, such as in the daya and jebel sites.

The dependence of growing season end on ERS was weak. This was likely affected by several factors. First, the results from a previous study show that ERS was more strongly associated with the timing when EVI2 starts to decrease [*Guan et al*., 2014b], but less correlated with the timing of EVI2 minimum (defined as growing season end). Second, plants in arid environments can be very tolerant to high-temperature and low-moisture conditions. Third, soil moisture could sustain plant growth after ERS. The discrepancy is supported by the result that the growing season end occurred after ERS in dryland ecosystems in the Sahel and Southern Africa [*Zhang et al*., 2005].

The regression analyses between LSP magnitudes (i.e., EVI2 amplitude and accumulated EVI2) and accumulated rainfall show that vegetation growth was more strongly controlled by the total rainfall received during the growing season and the preceding dormancy phases than by the accumulated rainfall during growing season alone. This is likely associated with the fact that rainfall occurring before the onset of growing season increases soil moisture which initiates bud-burst in perennial species and germination of annual species. Thus, the rainfall accumulated before onset of growing season contributes to EVI2 amplitude and accumulated EVI2. Further, the finding that EVI2 amplitude was more sensitive to accumulated rainfall than accumulated EVI2 is consistent with the result from a previous study in Australia's dry interior [*Broich et al*., 2014]. Moreover, the relatively low $R^2$ is likely related to the high variability in the response of LSP magnitudes to rainfall in dryland ecosystems [*Broich et al*., 2014; *Brown and de Beurs*, 2008; *Ma et al*., 2013]. In addition, the temporal distribution of rainfall might also have influences on LSP magnitudes. For example, a fixed amount of rainfall can be accumulated by a few strong storms or by many low-intensity rainfall events. The former might become runoff and do not make contribution to soil moisture accumulation.

## 6. Conclusions

Land surface phenology extracted from the SEVIRI EVI2 using the HPLM-LSPD algorithm revealed the occurrences of vegetation seasonality at a broad spatial scale across the Sahara desert. Overall, the characteristics of vegetation phenology in the Sahara desert differ significantly from those in other ecosystems. Specifically, vegetation growing season can unfold during dry seasons after growing season onset is triggered during

rainy seasons. Vegetation growing season can be as long as 300 days or more in some areas and years. EVI2 amplitude and accumulated EVI2, however, tends to be very low indicating sparse vegetation as expected in desert regions (EVI2 amplitude generally varied from 0.02 to 0.12 and accumulated EVI2 varied from 2.0 to 8.0 EVI2 units). EVI2 amplitude and accumulated EVI2 strongly depended on the total rainfall received during the growing season and the preceding dormancy period. In the southern Sahara desert, the spatial pattern in the timing of the growing season onset was driven by the onset of rainy season associated with the summer rainfall regime. Although no significant relationship between ORS and growing season onset was identified in the northern Sahara desert, the isolated rain storms in this region did seem to predominately occur during vegetation growing seasons. The end timing of a growing season revealed no significant dependence on that of the rainy season end. This is likely associated with dominance of weakly deciduous and perennial plants in the desert regions that maintain green leaf area well into the dry season, particularly in areas that benefit from rainfall redistribution to wadis, dayas, chotts/sebkhas, and jebels within the stony and rocky regions.

**Acknowledgments**
Xiaoyang Zhang acknowledged the supports from the NOAA GOES-R Risk Reduction Project GOES-R3#250, the NOAA contract JPSS_PGRR2_14, and NASA contracts NNX15AB96A. Any data used in this manuscript can be accessed by contacting the corresponding author. Felix Kogan at NOAA is thanked for his comments on the manuscript.

## References

Ali, M. M., G. Dickinson, and K. J. Murphy (2000), Predictors of plant diversity in a hyperarid desert wadi ecosystem, *J. Arid Environ.*, *45*(3), 215–230, doi:10.1006/jare.2000.0631.

Benhouhou, S. S., T. C. D. Dargie, and O. L. Gilbert (2003), Vegetation associations in the Ougarta Mountains and dayas of the Guir hamada, Algerian Sahara, *J. Arid Environ.*, *54*(4), 739–753, doi:10.1006/jare.2002.1070.

Broich, M., A. Huete, M. G. Tulbure, X. Ma, Q. Xin, M. Paget, N. Restrepo-Coupe, K. Davies, R. Devadas, and A. Held (2014), Land surface phenological response to decadal climate variability across Australia using satellite remote sensing, *Biogeosciences*, *11*, 5181–5198, doi:10.5194/bg-11-5181-2014.

Brown, M. E., and K. M. de Beurs (2008), Evaluation of multi-sensor semi-arid crop season parameters based on NDVI and rainfall, *Remote Sens. Environ.*, *112*(5), 2261–2271, doi:10.1016/j.rse.2007.10.008.

Burdette, C. (2001), Desert and xeric shrublands: Tibesti-Jebel Uweinat montane xeric woodlands. [Available at http://www.worldwildlife.org/ecoregions/pa1331, accessed 05 April 2015].

Buyantuyev, A., and J. Wu (2012), Urbanization diversifies land surface phenology in arid environments: Interactions among vegetation, climatic variation, and land use pattern in the Phoenix metropolitan region, USA, *Landscape Urban Plann.*, *105*(1–2), 149–159, doi:10.1016/j.landurbplan.2011.12.013.

Dall'Olmo, G., and A. Karnieli (2002), Monitoring phenological cycles of desert ecosystems using NDVI and LST data derived from NOAA-AVHRR imagery, *Int. J. Remote Sens.*, *23*(19), 4055–4071, doi:10.1080/01431160110115988.

de Beurs, K. M., and G. M. Henebry (2005), Land surface phenology and temperature variation in the International Geosphere–Biosphere Program high-latitude transects, *Global Change Biol.*, *11*(5), 779–790, doi:10.1111/j.1365-2486.2005.00949.x.

de Beurs, K. M., and G. M. Henebry (2008), War, drought, and phenology: Changes in the land surface phenology of Afghanistan since 1982, *J. Land Use Sci.*, *3*(2–3), 95–111, doi:10.1080/17474230701786109.

Dinku, T., P. Ceccato, K. Cressman, and S. J. Connor (2010), Evaluating detection skills of satellite rainfall estimates over desert locust recession regions, *J. Appl. Meteorol. Climatol.*, *49*(6), 1322–1332, doi:10.1175/2010JAMC2281.1.

El Kenawy, A. M., J. I. Lopez-Moreno, M. F. McCabe, and S. M. Vicente-Serrano (2015), Evaluation of the TMPA-3B42 precipitation product using a high-density rain gauge network over complex terrain in northeastern Iberia, *Global Planet. Change*, *133*, 188–200, doi:10.1016/j.gloplacha.2015.08.013.

European Organisation for the Exploitation of Meteorological Satellites (2012), Conversion from radiances to reflectances for SEVIRI warm channels, Rep. EUM/MET/TEN/12/0332, 8 pp. [Available at http://www.eumetsat.int/website/home/Data/Products/Calibration/MSGCalibration/index.html.]

Guan, K., D. Medvigy, E. F. Wood, K. K. Caylor, L. Shi, and J. Su-Jong (2014a), Deriving vegetation phenological time and trajectory information over Africa using SEVIRI daily LAI, *IEEE Trans. Geosci. Remote Sens.*, *52*(2), 1113–1130, doi:10.1109/tgrs.2013.2247611.

Guan, K., E. F. Wood, D. Medvigy, J. Kimball, M. Pan, K. K. Caylor, J. Sheffield, X. Xu, and M. O. Jones (2014b), Terrestrial hydrological controls on land surface phenology of African savannas and woodlands, *J. Geophys. Res. Biogeosci.*, *119*, 1652–1669, doi:10.1002/2013JG002572.

Harada, C., A. Sumi, and H. Ohmori (2003), Seasonal and year-to-year variations of rainfall in the Sahara desert region based on TRMM PR data, *Geophys. Res. Lett.*, *30*(6), 1288, doi:10.1029/2002GL016695.

Heumann, B. W., J. W. Seaquist, L. Eklundh, and P. Jönsson (2007), AVHRR derived phenological change in the Sahel and Soudan, Africa, 1982–2005, *Remote Sens. Environ.*, *108*(4), 385–392, doi:10.1016/j.rse.2006.11.025.

Huete, A. R., K. Didan, Y. E. Shimabukuro, P. Ratana, S. R. Saleska, L. R. Hutyra, W. Yang, R. R. Nemani, and R. Myneni (2006), Amazon rainforests green-up with sunlight in dry season, *Geophys. Res. Lett.*, *33*, L06405, doi:10.1029/2005GL025583.

Jiang, Z., A. R. Huete, K. Didan, and T. Miura (2008), Development of a two-band enhanced vegetation index without a blue band, *Remote Sens. Environ.*, *112*(10), 3833–3845, doi:10.1016/j.rse.2008.06.006.

Kariyeva, J., and W. Van Leeuwen (2011), Environmental drivers of NDVI-based vegetation phenology in Central Asia, *Remote Sens.*, *3*(2), 203.

Kelley, O. A. (2014), Where the least rainfall occurs in the Sahara desert, the TRMM radar reveals a different pattern of rainfall each season, *J. Clim.*, *27*(18), 6919–6939, doi:10.1175/JCLI-D-14-00145.1.

Liebmann, B., I. Bladé, G. N. Kiladis, L. M. V. Carvalho, G. B. Senay, D. Allured, S. Leroux, and C. Funk (2012), Seasonality of African precipitation from 1996 to 2009, *J. Clim.*, *25*(12), 4304–4322, doi:10.1175/jcli-d-11-00157.1.

Ma, X., et al. (2013), Spatial patterns and temporal dynamics in savanna vegetation phenology across the North Australian Tropical Transect, *Remote Sens. Environ.*, *139*, 97–115, doi:10.1016/j.rse.2013.07.030.

Mayaux, P., E. Bartholomé, S. Fritz, and A. Belward (2004), A new land-cover map of Africa for the year 2000, *J. Biogeogr.*, *31*(6), 861–877, doi:10.1111/j.1365-2699.2004.01073.x.

Merchant, C. J., A. R. Harris, E. Maturi, and S. Maccallum (2005), Probabilistic physically based cloud screening of satellite infrared imagery for operational sea surface temperature retrieval, *Q. J. R. Meteorol. Soc.*, *131*(611), 2735–2755, doi:10.1256/qj.05.15.

Milewski, A., R. Elkadiri, and M. Durham (2015), Assessment and comparison of TMPA satellite precipitation products in varying climatic and topographic regimes in Morocco, *Remote Sens.*, *7*(5), 5697.
Mitchell, C. W., and S. G. Willimott (1974), Dayas of the Moroccan Sahara and other arid regions, *Geogr. J.*, *140*(3), 441–453, doi:10.2307/1796537.
Nedjimi, B. (2012), Seasonal variation in productivity, water relations and ion contents of *Atriplexhalimus* spp. *schweinfurthii* grown in Chott *Zehrez* wetland, Algeria, *J. Saudi Soc. Agric. Sci.*, *11*(1), 43–49, doi:10.1016/j.jssas.2011.08.002.
Nedjimi, B., B. Beladel, and B. Guit (2012), Biodiversity of halophytic vegetation in Chott Zehrez Lake of Djelfa (Algeria), *Am. J. Plant Sci.*, *3*(11), 1527–1534, doi:10.4236/ajps.2012.311184.
Nicholson, S. E. (1981), Rainfall and atmospheric circulation during drought periods and wetter years in West Africa, *Mon. Weather Rev.*, *109*(10), 2191–2208, doi:10.1175/1520-0493(1981)109<2191:RAACDD>2.0.CO;2.
Nicholson, S. E. (2000), The nature of rainfall variability over Africa on time scales of decades to millenia, *Global Planet. Change*, *26*(1–3), 137–158, doi:10.1016/S0921-8181(00)00040-0.
Noy-Meir, I. (1973), Desert ecosystems: Environment and producers, *Annu. Rev. Ecol. Syst.*, *4*(1), 25–51, doi:10.1146/annurev.es.04.110173.000325.
Okin, G. S., N. Mahowald, O. A. Chadwick, and P. Artaxo (2004), Impact of desert dust on the biogeochemistry of phosphorus in terrestrial ecosystems, *Global Biogeochem. Cycles*, *18*, GB2005, doi:10.1029/2003GB002145.
Pekel, J. F., P. Ceccato, C. Vancutsem, K. Cressman, E. Vanbogaert, and P. Defourny (2011), Development and application of multi-temporal colorimetric transformation to monitor vegetation in the desert locust habitat, *IEEE J. Sel. Top. Appl. Earth Obs. Remote Sens.*, *4*(2), 318–326, doi:10.1109/JSTARS.2010.2052591.
Peng, B., J. Shi, W. Ni-Meister, T. Zhao, and D. Ji (2014), Evaluation of TRMM Multisatellite Precipitation Analysis (TMPA) products and their potential hydrological application at an arid and semiarid basin in China, *IEEE J. Sel. Top. Appl. Earth Obs. Remote Sens.*, *7*(9), 3915–3930, doi:10.1109/JSTARS.2014.2320756.
Renier, C., F. Waldner, D. Jacques, M. Babah Ebbe, K. Cressman, and P. Defourny (2015), A dynamic vegetation senescence indicator for near-real-time desert locust habitat monitoring with MODIS, *Remote Sens.*, *7*(6), –7545, doi:10.3390/rs70607545.
Safriel, U., et al. (2006), Deserts and the planet—Linkages between deserts and non-deserts, in *Global Deserts Outlook*, edited by E. Ezcurra, U. N. Environ. Programme, Nairobi.
Sagan, C., O. B. Toon, and J. B. Pollack (1979), Anthropogenic albedo changes and the Earth's climate, *Science*, *206*(4425), 1363–1368, doi:10.1126/science.206.4425.1363.
Sakkir, S., J. Shah, A. Cheruth, and M. Kabshawi (2015), Phenology of desert plants from an arid gravel plain in eastern United Arab Emirates, *J. Arid Land*, *7*(1), 54–62, doi:10.1007/s40333-014-0036-2.
Saleska, S. R., K. Didan, A. R. Huete, and H. R. da Rocha (2007), Amazon forests green-up during 2005 drought, *Science*, *318*(5850), 612, doi:10.1126/science.1146663.
Shmida, A. (1985), Biogeography of the desert floras of the world, in *Ecosystems of the World: Hot Deserts and Arid Shrublands*, edited by M. Evenari, I. Noy-Meir, and D. W. Goodall, pp. 1–30, Elsevier, Amsterdam.
Springuel, I., M. Sheded, F. Darius, and R. Bornkamm (2006), Vegetation dynamics in an extreme desert wadi under the influence of episodic rainfall, *Pol. Bot. Stud.*, *22*, 459–472.
Tian, Y., P. Romanov, Y. Yunyue, X. Hui, and D. Tarpley (2010), Analysis of vegetation index NDVI anisotropy to improve the accuracy of the GOES-R green vegetation fraction product, paper presented at Geoscience and Remote Sensing Symposium (IGARSS) 2010, 25–30 July.
Tielbörger, K., and R. Salguero-Gómez (2014), Some like it hot: Are desert plants indifferent to climate change?, in *Progress in Botany*, edited by U. Lüttge, W. Beyschlag and J. Cushman, pp. 377–400, Springer, Berlin, doi:10.1007/978-3-642-38797-5_12.
Vrieling, A., J. De Leeuw, and M. Y. Said (2013), Length of growing period over Africa: Variability and trends from 30 years of NDVI time series, *Remote Sens.*, *5*(2), 982–1000, doi:10.3390/rs5020982.
Walker, J., K. de Beurs, and R. Wynne (2015), Phenological response of an Arizona dryland forest to short-term climatic extremes, *Remote Sens.*, *7*(8), 10,832, doi:10.3390/rs70810832.
Zhang, X. (2015), Reconstruction of a complete global time series of daily vegetation index trajectory from long-term AVHRR data, *Remote Sens. Environ.*, *156*, 457–472, doi:10.1016/j.rse.2014.10.012.
Zhang, X., M. A. Friedl, C. B. Schaaf, A. H. Strahler, J. C. F. Hodges, F. Gao, B. C. Reed, and A. Huete (2003), Monitoring vegetation phenology using MODIS, *Remote Sens. Environ.*, *84*(3), 471–475, doi:10.1016/S0034-4257(02)00135-9.
Zhang, X., M. A. Friedl, C. B. Schaaf, A. H. Strahler, and Z. Liu (2005), Monitoring the response of vegetation phenology to precipitation in Africa by coupling MODIS and TRMM instruments, *J. Geophys. Res.*, *110*, D12103, doi:10.1029/2004JD005263.
Zhang, X., M. A. Friedl, and C. B. Schaaf (2006), Global vegetation phenology from Moderate Resolution Imaging Spectroradiometer (MODIS): Evaluation of global patterns and comparison with in situ measurements, *J. Geophys. Res.*, *111*, G04017, doi:10.1029/2006JG000217.
Zhang, X., D. Tarpley, and J. T. Sullivan (2007), Diverse responses of vegetation phenology to a warming climate, *Geophys. Res. Lett.*, *34*, L19405, doi:10.1029/2007GL031447.
Zhang, Y., et al. (2013), Extreme precipitation patterns and reductions of terrestrial ecosystem production across biomes, *J. Geophys. Res. Biogeosci.*, *118*, 148–157, doi:10.1029/2012JG002136.